International Journal of Mechanical Sciences 252 (2023) 108372

Contents lists available at ScienceDirect

International Journal of Mechanical Sciences

journal homepage: www.elsevier.com/locate/ijmecsci

Virtual modelling integrated phase field method for dynamic fracture analysis

Yiyang Liu [a], Yuan Feng [a,b,*], Di Wu [c], Xiaojun Chen [a], Wei Gao [a,*]

[a] Centre for Infrastructure Engineering and Safety (CIES), School of Civil and Environmental Engineering, The University of New South Wales, Sydney, NSW 2052, Australia
[b] School of Architecture and Built Environment, The University of Newcastle, Callaghan, NSW 2308, Australia
[c] Centre for Built Infrastructure Research (CBIR), School of Civil and Environmental Engineering, University of Technology Sydney, Sydney, NSW 2007, Australia

ARTICLE INFO

Keywords:
Non-deterministic damage prediction
Virtual modelling
Dynamic fracture mechanics
Phase field method

ABSTRACT

A non-deterministic phase field (PF) virtual modelling framework is proposed for three-dimensional dynamic brittle fracture. The developed framework is based on experimental observations, accurate numerical modelling, and virtually foreseeable dynamic fracture prediction module through the machine learning algorithm. The uncertain system inputs, including variabilities of material properties, are incorporated into dynamic fracture analysis. Phase field method is implemented to simulate the dynamic fracture behaviours of 3D cracked structures with variabilities and then to create the training database for virtual damage model. The virtual damage model omits the physical finite element approximation process and reveals the virtual governing relationship between the variational system inputs and fracture responses. This advantage enables the virtual model to provide reliable crack propagation prediction based on either experiment-based or numerical simulation and greatly improves the computational efficiency of dynamic fracture analysis. To establish the accurate virtual model in the training process, a newly developed extended support vector regression (X-SVR) method with T-spline polynomial kernel functions is adopted for its outstanding performance in handling complex high-dimensional problems. Based on different real-world engineering scenarios, multiple fracture failure criteria, both strength-based and serviceability-based, are selected and demonstrated in numerical investigations to visualise the proposed framework's workflow. The effectiveness as well as accuracy are verified by these examples, and it is observed that the computational efficiency of dynamic fracture analysis is greatly improved. With the proposed framework, a continuously updating dynamic fracture surveillance system can be potentially built for practical applications.

1. Introduction

Dynamic fracture problems are crucial to structural safety because modern structures frequently suffer from dynamic loadings like wind, earthquake, impact, and blast loads. Enormous efforts have been devoted to practical engineering applications for preventing dynamic fracture-induced failure, especially in high-value engineering projects [1,2] and newly-developed materials [3–5], with small-scale experiments [6–11] or simplified simulations. In the meantime, it's inevitable to consider the influence of variabilities in the design process, and massive experimental or numerical data is needed to generate the mathematical formula covering almost every possible combination. The dynamic loading condition is more complicated because of variational time-dependant parameters, thus numerical simulation turns out to be a better way in terms of computational cost and expense.

The energy approach was introduced into fracture mechanics by Griffith's theory [12,13] . In the later development of numerical fracture modelling, the standard finite element method (FEM) shows its capability with some theoretical innovations. This branch of FEM-based approaches is categorized as discrete model. In this branch, many methods have been proposed, such as the extended finite element method (XFEM) [14–16], the generalized finite element method (GFEM) [17]. In XFEM approach, the kinematics of finite elements is extended to incorporate the discontinuity with the suitable space. As mentioned,

* Corresponding authors at: Centre for Infrastructure Engineering and Safety (CIES), School of Civil and Environmental Engineering, The University of New South Wales, Sydney, NSW 2052, Australia.
E-mail addresses: yuan.feng1@unsw.edu.au (Y. Feng), w.gao@unsw.edu.au (W. Gao).

https://doi.org/10.1016/j.ijmecsci.2023.108372
Received 17 December 2022; Received in revised form 3 April 2023; Accepted 8 April 2023
Available online 10 April 2023

these approaches treat the crack as a strong discontinuity and try to represent the damage by crack tracking algorithms. A challenging problem arising in the discrete methods is the difficulty in solving complex crack patterns or crack initiation problems [18]. The other branch of the fracture modelling, the diffusive one, has been developed to smear the damage in the local area and to avoid introducing a sudden discontinuity in the displacement field. One representative approach is named as the phase field method (PFM). The phase field method is initially proposed by Francfort and Marigo [19] and Aranson et al. [20] in the beginning of 21st century. The variational approach mentioned in [19] applies Griffith's theory in finding the minimum total potential energy and then tracking the crack propagation. The numerical implementation of the variational approach was published by Bourdin et al. [21,22]. Then, Amor et al. [23] proposed the anisotropic model for disguising tensile and compressive stresses. Miehe et al. [24,25] achieved tremendous progress in the variational function framework and laid an essential foundation for further development. Recently, many researchers have flexibly implemented phase field modelling of brittle [26,27] and elasto-plastic fracture [28–35]. With a different constitutive law from regular materials, shape memory material arouses interests from researchers [36–38]. Although the dynamic phase field model has been formulated by Landau-Ginzburg type equations [39], Borden et al. [40] developed a more easy-understanding Bourdin-type formulations which are based on Griffith's theory. Furthermore, the fatigue fracture is studied in [41].

In the area of numerical application, Msekn et al. [42] and Molnar and Gravouil [43,44] successfully implemented the phase field method to ABAQUS with a user-defined subroutine (UEL). These methods with UEL codes simplify the solving process by adopting built-in solver in ABAQUS and offer an alternative way to modify different constitution laws for both brittle and ductile materials. In this paper, the phase field method is accomplished by adopting theoretical techniques from Molnar and developing dynamic brittle fracture with UEL.

Generally, PFM applies a scalar parameter in the introduced phase field to describe the material condition transiting from the intact one to the broken. So that the phase field method can represent a sharp crack without remeshing and skip assigning specific crack tracking algorithms. This character enables it to simulate complex crack propagation more naturally, including crack initiation, merging, or branching. This advantage is significant in dynamic fracture because crack patterns are much more complex and propagation process is harder to track under dynamic loads, especially when considering variabilities.

In this paper, phase field method with UEL codes is adopted in modelling dynamic brittle fracture considering variabilities. Although many researchers developed various methods to predict the crack propagation more precisely, the consideration of variabilities in fracture process will add an extra dimension to the original problem and will greatly increase the complexity. Thus, relevant research on non-deterministic dynamic fracture mechanics is very limited in the literatures.

In recent years, researchers have faced major challenges in the non-deterministic dynamic fracture modelling process. The first challenge is investigating the variational fracture performance of practical structures under dynamic loading. Unlike static fracture analysis, dynamic systems are more complex due to the additional time integration domain. Additionally, the implementation of variational input factors dramatically increases the complexity of the dynamic modelling framework, especially for three-dimensional cracked structures with a large number of degrees of freedom. Most of published research [45,46] on non-deterministic fracture modelling considers the randomness but limits the loading to static/quasi-static one. Recently, Feng et al. [47] used the machine learning method to improve the efficiency of static fracture problems. However, contemporary structures typically experience dynamic loading during their service periods, and quasi-static simulations are inadequate in this condition. Moreover, introducing randomness tremendously complicates the modelling process, and there are no solid studies on the qualification of variation's influence on dynamic fracture simulation. Traditional Monte Carlo simulations [48,49] are commonly used for uncertainty qualification in engineering problems, but applying them in dynamic fracture is difficult due to the large number of combinations from variational loading conditions, which leads to unacceptable computational efforts. The last major challenge is low computational efficiency of phase field method in dynamic fracture problems. Many researchers have published their achievements in raising the computational efficiency. Wu et al. [27] combined the optimizing algorithm BFGS in PFM, leading to quicker convergent speed in every step. Seles et al. [50] developed a residual control algorithm in ABAQUS implementation and adaptive algorithm is also popular for computational efficiency [51–58]. Samaniego et al. [59] develops a parallel implementation in ductile fracture with shear bands. Although these contributions have improved computational efficiency to some extent, phase field modelling of dynamic fracture remains time-consuming, and its efficiency is insufficient for non-deterministic dynamic fracture prediction. Modelling the millions of permutations and combinations of variational parameters requires millions of repetitive FE simulations, resulting in impractical computational costs. Therefore, significantly improving efficiency is a crucial factor in achieving non-deterministic dynamic fracture prediction.

In this paper, to efficiently characterize the non-deterministic dynamic fracture responses, a phase field (PF) virtual modelling framework with high accuracy is proposed. The variabilities should be analysed and configured quantitively in the first step. Material properties are considered as variational parameters for the widespread existence of unavoidable imperfections in engineering applications. The second step is conducting a limited number of necessary Monte Carlo simulations using the PFM-embedded Abaqus user subroutine codes (UEL). The phase field model can chase complex crack paths, including crack initiation or propagation and provide the origin training data for further generation of the virtual model. The training database connects fracture responses with each combination of variabilities at each time step. Therefore, the time discretization in the non-deterministic dynamic fracture is fully considered. Within the framework, the newly developed machine learning method, extended Support Vector Regression (X-SVR) [60,61] with T-spline kernel, is used to establish the virtual model. The virtual model reveals the virtual governing relationship between the system variabilities (i.e. variational material properties) and structural fracture responses (i.e. propagated crack length). Then, the target fracture responses can be obtained in an accurate and efficient manner by providing variation information to the well-trained virtual model. Based on the observed results, the virtual model can provide reliable fracture response predictions with new material property inputs, even out of the original input ranges. Finally, the virtual model can be applied to multiple tasks. This framework eliminates the high computational toll by virtual modelling and can generate a comprehensive structural health database without millions of repetitive MCS. Furthermore, this framework gives the possibility of rapid structure monitoring (diagnosis-prognosis) and provides real-time disaster warning when encountering dynamic loadings like severe wind or earthquake. Once the possible dynamic loads are predicted and quantified, fracture responses can be accessed within seconds and the estimated reliability data helps the decision maker to prevent personnel and property losses.

The outline of this paper is shown as follows. Section 2 illustrates the phase field theory of dynamic brittle fracture. In Section 3, the numerical implementation of the phase field method in the dynamic fracture problem is thoroughly reviewed. Variabilities are introduced into the fracture problem in this part as well. For better understanding, the virtual modelling framework of the phase field method is proposed in Section 4. In Section 5, two numerical examples are demonstrated to show the overall application process of the proposed framework. Finally, the general conclusion of this paper is discussed in Section 6.

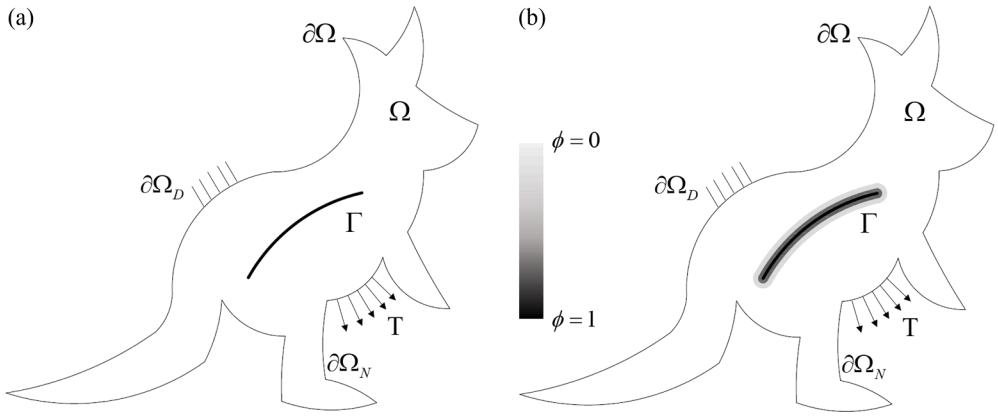

Fig. 1. (a) An elastic solid with sharp crack: the solid is under external boundary condition $\partial\Omega_D$ and the traction force **T**, the crack geometry is denoted as Γ ; (b) an elastic solid with geometrically regularized crack by phase field value ϕ: the phase field model diffuses the sharp crack into surrounding geometry.

2. Phase field method of dynamic brittle fracture

In this section, the basic introduction of phase field model is provided, and the corresponding theoretical information is explained. Generally, phase field method diffuses the crack geometry within the range formalised by an internal length (l_0) and then introduces a scalar value $\phi(\boldsymbol{x})$, where $\boldsymbol{x}$ is the position vector, to represent the intact-cracked transition of materials.

In the phase field method theory, an arbitrary body $\Omega \subset \mathbb{R}^d (d = \{1, 2, 3\})$ is considered, which has an external boundary condition $\partial\Omega$ and an internal discontinuity boundary Γ, as shown in Fig. 1. At the time t, the displacement $\boldsymbol{u}(\boldsymbol{x}, t)$ satisfies the Neumann boundary conditions on $\partial\Omega_N$ and Dirichlet boundary conditions on $\partial\Omega_D$. The traction force $\mathbf{T}(\boldsymbol{x}, t)$ is applied to the boundary $\partial\Omega_N$.

The mentioned scalar variable $\phi(\boldsymbol{x}) \in [0, 1]$ is called phase field value, and it's adopted to represent the status of the elastic body by,

$$\phi(\boldsymbol{x}) = \begin{cases} 0 & \text{Intact} \\ 1 & \text{Cracked} \end{cases} \tag{1}$$

According to Griffith's theory [62], a variation approach has been taken to solve the fracture problem [21,24,25]. The critical fracture energy release rate G_c is defined as the minimum required energy to create a new fracture surface per unit area. Then, the weak form of the governing equations of the cracked domain can be developed with total potential energy. The total potential energy $\Psi_{pot}(\boldsymbol{u},\Gamma)$ can be expressed by the elastic energy Ψ_ε, fracture energy Ψ_{frac} and external forced energy Ψ_{ext}:

$$\begin{aligned} \Psi_{pot}(\boldsymbol{u},\Gamma) &= \Psi_\varepsilon + \Psi_{frac} - \Psi_{ext} \\ &= \int_\Omega \psi_{\boldsymbol{\varepsilon}}(\boldsymbol{\varepsilon}) d\Omega + \int_\Gamma G_c(\boldsymbol{x}) d\Gamma - \int_{\partial\Omega_N} \mathbf{T}\cdot\boldsymbol{u}\, d\partial\Omega_N \end{aligned} \tag{2}$$

where the linear strain tensor $\boldsymbol{\varepsilon} = \boldsymbol{\varepsilon}(\boldsymbol{u})$ can be expressed by:

$$\boldsymbol{\varepsilon}_{ij} = \frac{1}{2}\left(\frac{\partial \boldsymbol{u}_i}{\partial x_j} + \frac{\partial \boldsymbol{u}_j}{\partial x_i}\right) \tag{3}$$

Under the assumption of anisotropic linear elasticity, the linear energy density $\psi_\varepsilon(\varepsilon)$ is proposed by Miehe et al. [25] with Lamé constants λ and μ as:

$$\psi_{\boldsymbol{\varepsilon}}(\boldsymbol{\varepsilon}) = \frac{1}{2}\lambda \boldsymbol{\varepsilon}_{ii}\boldsymbol{\varepsilon}_{jj} + \mu \boldsymbol{\varepsilon}_{ij}\boldsymbol{\varepsilon}_{ij} \tag{4}$$

The elastic strain energy density can be decomposed into the tensile strain energy density $\psi_{\boldsymbol{\varepsilon}}(\boldsymbol{\varepsilon})^+$and the compressive strain energy density $\psi_{\boldsymbol{\varepsilon}}(\boldsymbol{\varepsilon})^-$, where only the tensile part will be degraded because of the existence of a crack [23,63]. It should be noted that, the positive and negative strain energy density is calculated from the corresponding strain tensor according to Miehe et al. [25]. In his theory, the spectral decomposition of the strain tensor is,

$$\boldsymbol{\varepsilon} = \sum_{i=1}^{3} \boldsymbol{\varepsilon}_i \boldsymbol{n}_i \otimes \boldsymbol{n}_i \tag{5}$$

where $\{\boldsymbol{\varepsilon}_i\}_{i\,=\,1,\,2,\,3}$ are the principal strains and $\{\boldsymbol{n}_i\}_{i\,=\,1,\,2,\,3}$ are the principal strain directions. In this process, the shear strains have been already considered in the formation of principle strains. A degradation function containing the phase field value reduces the tensile strain energy density. The degradation function $g(\phi)$ is formulated by:

$$g(\phi) = (1 - \phi(\boldsymbol{x}))^2 + k \tag{6}$$

where k is a small number (10^{-7}) introduced for numerical stability when $\phi(\boldsymbol{x}) \to 1$. The elastic energy is then written as:

$$\begin{aligned} \Psi_\varepsilon(\varepsilon) &= \int_\Omega \psi_\varepsilon(\boldsymbol{\varepsilon}) d\Omega \\ &= \int_\Omega \left[(1 - \phi(\boldsymbol{x}))^2 + k\right]\cdot\psi_\varepsilon(\boldsymbol{\varepsilon})^+ + \psi_\varepsilon(\boldsymbol{\varepsilon})^- d\Omega \end{aligned} \tag{7}$$

Based on the definition of phase field value, the surface is perfectly intact when $\phi(\boldsymbol{x}) = 0$ and damaged when $\phi(\boldsymbol{x}) = 1$. Then, another critical variable in the phase field model is introduced and named the length parameter l_0, which determines the width of the diffused region around the discontinuity. Miehe et al. [24] proposed the formulation describing the crack surface density per unit volume of solid as:

$$\gamma(l_0, \phi, \nabla\phi) = \frac{1}{2l_0}\cdot\phi(\boldsymbol{x})^2 + \frac{l_0}{2}\cdot|\nabla\phi(\boldsymbol{x})|^2 \tag{8}$$

With the crack surface density function (8), the fracture energy can be easily written as:

$$\begin{aligned} &\int_\Gamma G_c(x) d\Gamma \approx \int_\Omega G_c(\boldsymbol{x})\cdot\gamma(l_0, \phi, \nabla\phi) d\Omega \\ &= \int_\Omega G_c(\boldsymbol{x})\cdot\frac{1}{2l_0}\cdot\phi(\boldsymbol{x})^2 + \frac{l_0}{2}\cdot|\nabla\phi(\boldsymbol{x})|^2 d\Omega \end{aligned} \tag{9}$$

Combining formula (7) and (9), the total potential energy can be expressed as:

$$\begin{aligned} \Psi_{pot}(\boldsymbol{u},\Gamma) &= \int_\Omega \psi_{\boldsymbol{\varepsilon}}(\boldsymbol{\varepsilon}) d\Omega + \int_\Gamma G_c(\boldsymbol{x}) d\Gamma - \int_{\partial\Omega_N} \mathbf{T}\cdot\boldsymbol{u}\, d\partial\Omega_N \\ &= \int_\Omega \left[(1 - \phi(\boldsymbol{x}))^2 + k\right]\cdot\psi_{\boldsymbol{\varepsilon}}(\boldsymbol{\varepsilon})^+ + \psi_{\boldsymbol{\varepsilon}}(\boldsymbol{\varepsilon})^- d\Omega \\ &\quad + \int_\Omega G_c(\boldsymbol{x})\cdot\frac{1}{2l_0}\cdot\phi(\boldsymbol{x})^2 + \frac{l_0}{2}\cdot|\nabla\phi(\boldsymbol{x})|^2 d\Omega - \int_{\partial\Omega_N} \mathbf{T}\cdot\boldsymbol{u}\, d\partial\Omega_N \end{aligned} \tag{10}$$

The overall energy functional of dynamic fracture involves the Lagrange function:

$$L = D(\dot{\boldsymbol{u}}) - \Psi_{pot} \tag{11}$$

where $\dot{\mathbf{u}}$ contains the velocity vector and $D(\dot{\boldsymbol{u}})$ is the kinetic energy can be written with material density ρ:

$$D(\dot{\boldsymbol{u}}) = \frac{1}{2}\int_{\Omega} \dot{\boldsymbol{u}}^T \dot{\boldsymbol{u}} \rho d\Omega \tag{12}$$

Given the Lagrange functional, the governing equations of the dynamic fracture in terms of kinetic energy and potential energy can be simply developed.

Miehe et al. [24] developed a stagger scheme, which implies a history field to decouple the displacement field and phase field. This scheme allows us to embed the phase field model into Abaqus [43,44]. The fundamental algorithm of this scheme is to link the displacement field and phase field by a history field rather than coupled functions. In each iteration, the displacement field is solved firstly by applying the energy function:

$$\begin{aligned} \Pi_{\mathbf{u}} &= D(\dot{\boldsymbol{u}}) - \Psi_{\boldsymbol{\varepsilon}}(\boldsymbol{\varepsilon}) + \Psi_{ext} \\ &= \frac{1}{2}\int_{\Omega} \dot{\mathbf{u}}^T \dot{\mathbf{u}} \rho d\Omega - \int_{\Omega} \left[(1-\phi(\boldsymbol{x}))^2 + k\right] \cdot \psi_{\boldsymbol{\varepsilon}}(\boldsymbol{\varepsilon})^+ \\ &\quad + \psi_{\boldsymbol{\varepsilon}}(\boldsymbol{\varepsilon})^- d\Omega + \int_{\partial\Omega_N} \mathbf{T} \cdot \boldsymbol{u} d\partial\Omega_N \end{aligned} \tag{13}$$

Taking the first variation of (13), the corresponding strong form is:

$$\begin{aligned} \sigma \cdot \mathbf{n} - T &= 0 \quad \text{on } \partial\Omega_N \\ \nabla\phi \cdot \mathbf{n} &= 0 \quad \text{on } \partial\Omega_C \\ \boldsymbol{u} &= \overline{\boldsymbol{u}} \quad \text{on } \partial\Omega_D \end{aligned} \tag{14}$$

where $\mathbf{n}$ represents the outwards normal vectors on the boundary and the Cauchy stress tensor $\sigma = \frac{\partial \psi_{\boldsymbol{\varepsilon}}(\boldsymbol{\varepsilon})}{\partial \boldsymbol{\varepsilon}}$.

The strain history field $H(\boldsymbol{x})$ is then obtained by:

$$H(\boldsymbol{x}) = \max \psi_{\boldsymbol{\varepsilon}}^+(\boldsymbol{\varepsilon}(\boldsymbol{x})) \tag{15}$$

The function (15) automatically avoids the healing of cracks, and the initial condition for the history field is 0 ($H_0 = 0$). The Lagrange functional for phase field can be written as (16) by replacing $\psi_{\boldsymbol{\varepsilon}}(\boldsymbol{\varepsilon})^+$ with $H(\boldsymbol{x})$.

$$\Pi_{\phi} = \int_{\Omega} [G_c(\boldsymbol{x}) \cdot \gamma(l_0, \phi, \nabla\phi) + g(\phi) H(\boldsymbol{x})] d\Omega \tag{16}$$

The history field satisfies the Karush-Kuhn-Tucker condition since the irreversibility of $H(\boldsymbol{x})$. Thus, the strong form of phase field can be written as:

$$\begin{aligned} &\frac{G_c}{l_0}\left(\phi - l_0^2 \nabla\phi\right) = 2(1-\phi)H \quad \text{on } \partial\Omega_N \\ &\nabla\phi \cdot \mathbf{n} = 0 \qquad\qquad\qquad\quad \text{on } \partial\Omega_C \end{aligned} \tag{17}$$

3. Non-deterministic numerical implementation

In this section, the non-deterministic numerical implementation of dynamic phase field model is carefully explained. The application of ABAQUS with UEL codes is also clarified. Not surprisingly, the stochastic problem will introduce system variabilities into the governing equations, making them complex to solve. The dynamic fracture considering variabilities lead to unstable crack propagation.

Under these conditions, the monolithic scheme is not numerically reliable as it calculates the entire crack propagation route within a single time step. Therefore, the staggered time-integration algorithm is adopted to solve the stochastic dynamic fracture problem in this paper.

The Abaqus user subroutine options are used to solve the displacement field and phase field iteratively. For dynamic cases, Abaqus adopts the Hilber-Hughes-Taylor (HHT) method, a more common case of the New-mark method, to acquire the equilibrium. HHT is a built-in solver and solves the linearised equilibrium by Newton-Raphson iteration. No special calibrations should be taken when applying.

Table 1
Considered variabilities.

Variational parameters	Abbreviations	Unit
Young's modulus	$E(\boldsymbol{\eta}_j^R)$	GPa
Poisson's ratio	$\upsilon(\boldsymbol{\eta}_j^R)$	/
Critical energy release rate	$G_c(\boldsymbol{\eta}_j^R)$	J/m^2
Density	$\rho(\boldsymbol{\eta}_j^R)$	kg/m^3

The considered variabilities are material properties listed in Table 1. These variational parameters are assembled in a vector $\boldsymbol{\eta}^R = [E,\ \upsilon,\ G_c,\ \rho]^T$ [64,65]. In this framework, $\boldsymbol{\eta}_j^R$ represents the jth variational parameter set, and the vector $\boldsymbol{\eta}^R$ belongs to the probability space (Υ, Λ, P) where Υ denotes the sample space, Λ denotes the σ-algebra and P denotes the probability measure. The phase field model considers variational parameters, affecting the finite element discretization by influencing the stiffness matrix.

The linearised equilibrium at the time t_n considering the variabilities is written as:

$$\begin{aligned} &\begin{bmatrix} S_n^u\left(\boldsymbol{\eta}_j^R\right) & 0 \\ 0 & (1+\alpha)\mathrm{K}_n^d\left(\boldsymbol{\eta}_j^R\right) \end{bmatrix} \begin{bmatrix} u_{n+\Delta t}\left(\boldsymbol{\eta}_j^R\right) \\ \phi_{n+\Delta t}\left(\boldsymbol{\eta}_j^R\right) \end{bmatrix} \\ &= -\begin{bmatrix} r_n^u\left(\boldsymbol{\eta}_j^R\right) \\ \alpha r_{n-1}^d\left(\boldsymbol{\eta}_j^R\right) - (1+\alpha) r_n^d\left(\boldsymbol{\eta}_j^R\right) \end{bmatrix} \end{aligned} \tag{18}$$

where $\mathrm{S}_n^u(\boldsymbol{\eta}_j^R) = \mathrm{M}(\boldsymbol{\eta}_j^R)\frac{d\ddot{u}}{du} + (1+\alpha)\mathrm{K}_n^u(\boldsymbol{\eta}_j^R)$ and $K_n^d(\boldsymbol{\eta}_j^R)$ are the elementary stiffness in displacement field and phase field at a time step $\boldsymbol{\eta}_j^R$. $u_{n+\Delta t}(\boldsymbol{\eta}_j^R)$ and $\phi_{n+\Delta t}(\boldsymbol{\eta}_j^R)$ are new nodal solutions for the next time step $t_n + \Delta t$.

In this paper, the 3D 8-node brick element is considered in numerical implementation, meaning the shape functions $N = [N_1 \cdots N_8]$. The spatial derivatives can be written as:

$$B = \begin{bmatrix} \frac{\partial N_1}{\partial x} & \cdots & \frac{\partial N_8}{\partial x} \\ \frac{\partial N_1}{\partial y} & \cdots & \frac{\partial N_8}{\partial y} \\ \frac{\partial N_1}{\partial z} & \cdots & \frac{\partial N_8}{\partial z} \end{bmatrix} \tag{19}$$

Thus, N^u, N^ϕ are denoted for the shape function in the stochastic displacement field and phase field. B^u and B^ϕ are the derivatives for two fields correspondingly.

The elementary stiffness matrix in the displacement field can be calculated as:

$$K_n^u\left(\boldsymbol{\eta}_j^R\right) = \int_{\Omega} \left\{ \left[(1-\phi)^2 + k\right] (B^u)^T C_0\left(\boldsymbol{\eta}_j^R\right) B^u \right\} d\Omega \tag{20}$$

where C_0 is the stochastic elemental elastic stiffness matrix.

The elementary stiffness matrix in the phase field can be calculated as:

$$K_n^d\left(\boldsymbol{\eta}_j^R\right) = \int_{\Omega} \left\{ \left(N^\phi\right)^T \left[\frac{G_c\left(\boldsymbol{\eta}_j^R\right)}{l_0} + 2H\right] N^\phi + \left(B^\phi\right)^T G_c\left(\boldsymbol{\eta}_j^R\right) l_0 B^\phi \right\} d\Omega \tag{21}$$

In dynamic cases, the residual vector in displacement r_n^u should contain an inertial component which can be denoted as $\mathbf{f}_n^a$. In each increment, the elementary function of inertial force is written as:

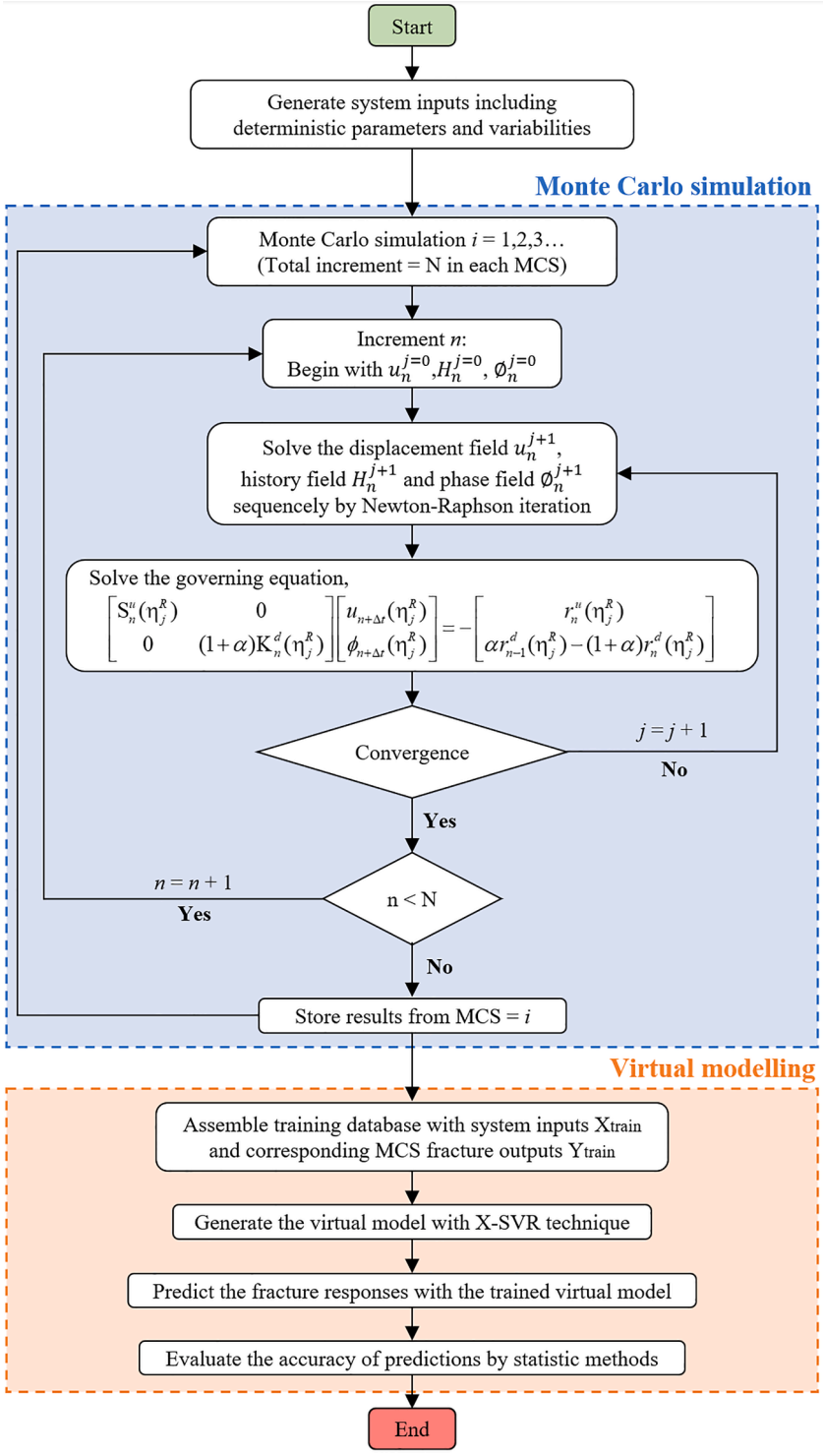

Fig. 2. Flowchart of non-deterministic phase field virtual modelling framework.

$$\mathbf{f}^a = \mathbf{f}_i^a = \int_\Omega \rho\left(\boldsymbol{\eta}_j^R\right) N_{ij}^u \ddot{\mathbf{u}} d\Omega \tag{22}$$

where i is element number and $N_{ij}^u(\boldsymbol{\eta}_j^R)$ is the matrix of shape functions in displacement problem containing the jth set of variabilities.

Similarly, the external and internal force vectors are identified as $\mathbf{f}_n^{ex}$ and $\mathbf{f}_n^{in}$.

$$\begin{aligned} \mathbf{f}_n^{ex} &= \int_\Omega (N^u)^T \mathrm{T} d\Omega \\ \mathbf{f}_n^{in} &= \int_\Omega \left\{ \left[(1-\phi)^2 + k \right] (B^u)^T \sigma \right\} d\Omega \end{aligned} \tag{23}$$

Considering the damping coefficient α, the displacement residual at time step t_n can be written in terms of:

$$r_n^u = (1+\alpha)\mathbf{f}_n^{in} - \alpha \mathbf{f}_{n-1}^{in} + \mathbf{f}_n^a - \mathbf{f}_n^{ex} \tag{24}$$

where the damping factor is taken as $\alpha = -0.05$.

The mass matrix can be written in a diagonal format as:

$$\mathbf{M} = M_{kk} = \int_{\Omega} \left(N_{kj}^{u}\right)^{T} \rho\left(\boldsymbol{\eta}_{j}^{R}\right) N_{kj}^{u} d\Omega \tag{25}$$

When variability is introduced into the numerical implementation, the governing equations of dynamic fracture become complex and extremely difficult to solve efficiently, particularly in 3D cases. The randomness of material properties has a significant impact on the fracture response, including crack propagation speed and direction. The difficulty of the traditional approach to solving these equations suggests the possibility of using a virtual modelling technique. Therefore, a stochastic analysis framework of the phase field method in the dynamic fracture is proposed, and the advanced virtual modelling technique is implemented to deal with the variational nonlinear problem involving high complexity.

4. Virtual modelling framework of phase field method

Due to the extremely high demand for computational capacity in non-deterministic 3D dynamic fracture problems with various variabilities, the newly developed virtual modelling technique is adopted and illustrated in this chapter.

4.1. Non-deterministic phase field method framework

The virtual modelling technique presents enormous advantages in dealing with the nonlinear variation problem. This paper proposes the non-deterministic phase field method framework for 3D dynamic problems. The novel virtual modelling method, extended support vector regression (X-SVR), works as the connection between the inputs and outputs. Given the newly generated input-output virtual relationship, the fracture responses from variational inputs can be easily and rapidly obtained.

Under the non-deterministic phase field method framework, the basic procedure is based on Monte Carlo simulation, and the staggered scheme is adopted in each set of variabilities. The flow chart is given in Fig. 2 to demonstrate the process more vividly. The variational parameters are generated according to the premise. Both the deterministic and non-deterministic parameters are collected and stored in the database for input data. For each input dataset η_j^R, the fracture responses (i.e., crack propagation length, failure time) can be read from the results file. The training dataset consists of variabilities and fracture responses. Then, the virtual modelling technique X-SVR works as the generator of the virtual relationship between input and output. After the generation of the well-trained X-SVR virtual model, fracture predictions can be made without solving complex governing equations.

4.2. Extended support vector regression

The virtual model in the stochastic phase field method of dynamic fracture is generated by regression based on the training data. It's critical to choose a suitable route so that the virtual model can predict more reliable fracture responses. The extended support vector regression is a robust and self-adaptive scheme. The extended support vector regression is developed from traditional SVR or DrSVM (doubly regularised support vector regression) [66–68] and achieves better training stability and performance by applying the quadratic ε-insensitive loss function. To handle the complexity of training data, mapping function $\zeta(\mathbf{x})$ is implemented in the framework. Typically, the kernelized mapping process is described by:

$$\mathbf{x}_i = \left[x_{i,1}, x_{i,2}, \cdots, x_{i,n}\right]^T \mapsto \widehat{w}(\mathbf{x}_i) = \begin{bmatrix} \zeta(\mathbf{x}_1)^T \zeta(\mathbf{x}_i) \\ \zeta(\mathbf{x}_2)^T \zeta(\mathbf{x}_i) \\ \vdots \\ \zeta(\mathbf{x}_n)^T \zeta(\mathbf{x}_i) \end{bmatrix} = \mathbf{W}(\mathbf{x}_i) \tag{26}$$

where n represents the number of training samples and $\mathbf{W}(\mathbf{x}_i)$ is kernelized mapping function.

Thus, the original training dataset will be mapped into high dimensional space $\mathbf{W}_{train}(\mathbf{x}_i)$ like:

$$\mathbf{W}_{train} = \begin{bmatrix} \mathbf{W}(\mathbf{x}_1, \mathbf{x}_1) & \mathbf{W}(\mathbf{x}_1, \mathbf{x}_2) & \cdots & \mathbf{W}(\mathbf{x}_1, \mathbf{x}_j) \\ \mathbf{W}(\mathbf{x}_2, \mathbf{x}_1) & \mathbf{W}(\mathbf{x}_2, \mathbf{x}_2) & \cdots & \mathbf{W}(\mathbf{x}_2, \mathbf{x}_j) \\ \vdots & \vdots & \ddots & \vdots \\ \mathbf{W}(\mathbf{x}_j, \mathbf{x}_1) & \mathbf{W}(\mathbf{x}_j, \mathbf{x}_1) & \cdots & \mathbf{W}(\mathbf{x}_j, \mathbf{x}_j) \end{bmatrix} \tag{27}$$

Within the mapped high-dimensional space, the X-SVR technique can be achieved by dealing with the optimization problem:

$$\min_{\mathbf{p}_x, \mathbf{q}_x, \lambda, \theta, \hat{\theta}} : \frac{\delta_1}{2}\left(\| \mathbf{p}_x \|_2^2 + \| \mathbf{q}_x \|_2^2\right) + \delta_2 \mathbf{e}_j^T (\mathbf{p}_x + \mathbf{q}_x) + \frac{z}{2}\left(\theta^T \theta + \widehat{\theta}^T \widehat{\theta}\right) \tag{28}$$

$$s.t. \begin{cases} \mathbf{W}_{train}(\mathbf{p}_x - \mathbf{q}_x) - \lambda \mathbf{e}_j - \mathbf{y}_{train} \le \omega \mathbf{e}_j + \theta \\ \mathbf{y}_{train} - \mathbf{W}_{train}(\mathbf{p}_x - \mathbf{q}_x) + \lambda \mathbf{e}_j \le \omega \mathbf{e}_j + \widehat{\theta} \\ \mathbf{p}_x, \mathbf{q}_x, \theta, \widehat{\theta} \ge 0^j \end{cases} \tag{29}$$

where $\mathbf{p}_x$, $\mathbf{q}_x$ are positive parameters for identifying the normal to the hyperplane; δ_1, δ_2 indicates the tunning parameters for feature selection; x donates the mapping procedure; θ, $\widehat{\theta}$ are the slack variables for allowing some excess deviations; $\mathbf{e}_j$ is a unit vector; λ donates the bias parameter; ω is introduced for the acceptable deviation in predicting function and training data.

Continuously, the X-SVR functions can be modified into pair of optimization problems:

$$\begin{aligned} &\min_{\mathbf{y}_x, \lambda} : \frac{1}{2}\left(\mathbf{y}_x^T \widehat{\mathbf{D}}_x \mathbf{y}_x + \lambda^2\right) + \delta_2 \mathbf{b}_x^T \mathbf{t}_x \\ &s.t. \left(\widehat{\mathbf{S}}_x + \mathbf{I}_{4j \times 4j}\right)\mathbf{t}_x + \left(\omega \mathbf{I}_{4j \times 4j} + \lambda \widehat{\mathbf{K}}_x\right)\widehat{\mathbf{e}}_x + \widehat{\mathbf{v}}_x \ge \mathbf{0}_{4j} \end{aligned} \tag{30}$$

where $\mathbf{I}_{4j \times 4j}$ is the identity matrix and $\mathbf{0}_{4j}$ is zero vector. The definition of related matrix can be found in Appendix A.

The optimization problem can be equivalently solved in the dual formulation by applying the Lagrange method with KKT conditions. Assuming the Lagrange multiplier $\varsigma_x \in \Re^{4j}$, the quadratic programming problem will be organised as:

$$\begin{aligned} &\min_{\varsigma_x} : \frac{1}{2}\boldsymbol{\varsigma}_x^T \mathbf{L}_x \boldsymbol{\varsigma}_x - \mathbf{r}_x^T \boldsymbol{\varsigma}_x \\ &s.t. \boldsymbol{\varsigma}_x \ge \mathbf{0}_{4j} \end{aligned} \tag{31}$$

where

$$\mathbf{L}_x = \left(\widehat{\mathbf{S}}_x + \mathbf{I}_{4j \times 4j}\right)\widehat{\mathbf{D}}_x^{-1}\left(\widehat{\mathbf{S}}_x + \mathbf{I}_{4j \times 4j}\right)^T + \widehat{\mathbf{K}}_x \widehat{\mathbf{e}}_x \widehat{\mathbf{e}}_x^T \widehat{\mathbf{K}}_x \tag{32}$$

$$\mathbf{r}_x^T = \delta_2 \mathbf{b}_x^T \widehat{\mathbf{D}}_x^{-1}\left(\widehat{\mathbf{S}}_x + \mathbf{I}_{4j \times 4j}\right)^T - \omega \widehat{\mathbf{e}}_x^T - \widehat{\mathbf{v}}_x^T \tag{33}$$

If ς_x^* is assumed as the solution for the Eq. (31), then the variable $\mathbf{t}_x$ and λ can be illustrated as:

$$\mathbf{t}_x = \widehat{\mathbf{D}}_x^{-1}\left(\left(\widehat{\mathbf{S}}_x + \mathbf{I}_{4j \times 4j}\right)^T \varsigma_x^* - \delta_2 \mathbf{b}_x\right) \tag{34}$$

$$\lambda = \widehat{\mathbf{e}}_x^T \widehat{\mathbf{K}}_x \varsigma_x^* \tag{35}$$

Then the coefficient $\mathbf{w}$ can be defined as:

$$\mathbf{w} = \mathbf{p}_x - \mathbf{q}_x = \mathbf{t}_x(1:j) - \mathbf{t}_x(j+1:2j) \tag{36}$$

The nonlinear regression function by X-SVR can be written as:

$$\widehat{f}(\mathbf{x}) = (\mathbf{p}_x - \mathbf{q}_x)^T \widehat{w}(\mathbf{x}) - \widehat{\mathbf{e}}_x^T \widehat{\mathbf{K}}_x \varsigma_x^* \tag{37}$$

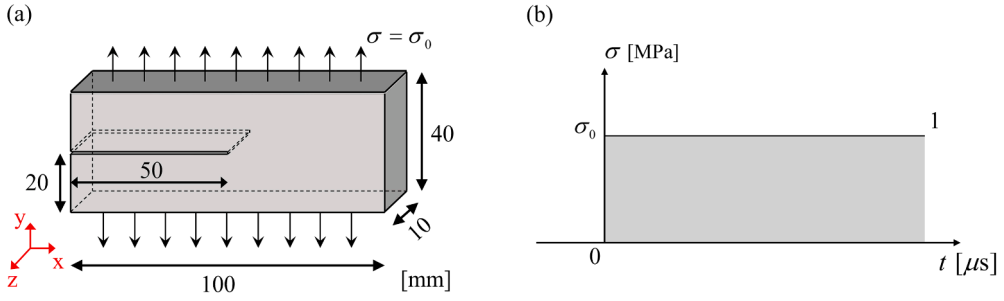

Fig. 3. (a) Geometric and boundary conditions of dynamic branching test; (b) load history information.

The Gaussian and polynomial kernels are quite popular in the SVR process [69], but their capacity to handle complex functions is not satisfied. Sometimes the regression results are not stable and reasonable. To overcome this disadvantage, the spline kernels [70] have been adopted when dealing with function estimation or non-parametric regression. The spline kernels can precisely capture local data trends and construct the overall regression function with polynomial basis functions. The popular B-spline kernel shows its compact support and stability in various numerical tests. Recently, T-spline functions have aroused much attention because of their extraordinary capacity for locally smooth refining in high-dimensional polynomial degrees. A new T-spline polynomial kernel function for the proposed kernelized XSVR is developed in this part. The T-spline polynomial kernel function $\mathbf{T}_{spline}(\zeta_i, \zeta_j)$ can be defined as:

$$\mathbf{T}_{spline}(\zeta_i, \zeta_j) = \frac{S_i d_i B_{2n+1}(\zeta_i - \zeta_j)}{\sum_{j=1}^{m} d_j B_{2n+1}(\zeta_i - \zeta_j)} \tag{38}$$

and

$$B_n(\zeta_i) = \sum_{r=0}^{i+1} \frac{(-1)^r}{i!} \cdot \frac{(i+1)!}{r!(i+1-r)!} \cdot \left(\zeta_i + \frac{i+1}{2} - r\right)_{\max}^{!} \tag{39}$$

where d_i is a set of positive weights of basis function; S_i represents the spline coefficient; $B_n(\zeta_i)$ is a B-spline kernel function; n is the order of polynomial.

According to the function (39), it's obvious that the order n significantly impacts the regression results. Therefore, the Bayesian optimization algorithm is embedded in the kernel algorithm for better performance of the proposed T-spline kernelized XSVR.

5. Numerical investigations

This paper aims to conduct non-deterministic fracture analysis of 3D structures based on the phase field method and demonstrate the effectiveness and efficiency of the implementation through the investigation of two typical examples involving variability.

5.1. 3D dynamic branching test

In the first numerical example, the benchmark dynamic branching test in the 3D version is illustrated and verified against former research results from Borden et al. [40] and Nguyen and Wu [71]. The material variabilities are considered in simulation to verify the effectiveness and efficiency of the proposed virtual modelling fracture analysis framework.

The geometry and boundary conditions of branching test can be found in Fig. 3. Outward thickness is 10 mm. There's an existing crack in the middle plane, and the pre-crack reaches the centre of the brick. The brick is loaded dynamically by uniform traction across the top and bottom surfaces. The traction load remains constant throughout the simulation. All the rest surfaces are under zero traction conditions. In this case, the crack should propagate in a straight line, and crack branching will occur.

Table 2
Variational material properties of dynamic branching test.

Variational parameters	Mean	Standard deviation	Distribution type	Range
ρ [kg/m^3]	2450	50	Normal	/
E [GPa]	32e9	3e9	Lognormal	/
υ	0.2	0.005	Uniform	[0.195, 0.205]
G_c [J/m^2]	3	0.1	Uniform	[2.95, 3.0]

The variational material properties are considered to simulate the inevitable manufacturing tolerance and artificial errors in the real engineering world. Four material variabilities are included in this simulation: density ρ, Young's modulus E, Poisson's ratio υ and critical energy release rate G_c. In order to verify the numerical model firstly, these material properties are set the same as in [40]: $\rho = 2450$ kg/m^3; $E = 32$ GPa; $\upsilon = 0.2$; $G_c = 3$ J/m^2.

These determined material properties are set as the mean value of non-deterministic processes, and the detailed statistical information of four independent variabilities is listed in Table 2.

To keep the balance of computational toll and result accuracy, the uniform mesh size in this 3D model is chosen as $h_{\min} = 0.5$ mm. The length scale parameter should be set as 1 mm for the accuracy of phase field model. Therefore, a total number of 126,375 nodes and 114,128 quadrangle elements are generated in the 3D numerical model. The step size is $\Delta t = 1 \times 10^{-8}$ s while the total simulation time $t_{\text{total}} = 1 \times 10^{-4}$ s.

In the first step, the results from the chosen mean value of material properties are compared to the former publications for validation. The crack propagation plot is a vital tool for checking the correctness of numerical model. As shown in Fig. 4, the 3D crack propagation demonstrates the same pattern in Borden's model, but the crack width is more significant. The difference is caused by the chosen length parameter.

Additionally, elastic strain and dissipated energy plots are plotted and compared with results in [40,71], as shown in Fig. 5. The relative error amongst the results can be acceptable because a coarser mesh setting is adopted in the simulated 3D model.

In the first step, the results from the chosen mean value of material properties are compared to the former publications for validation. The crack propagation plot is a vital tool for checking the correctness of numerical model. As shown in Fig. 4, the 3D crack propagation demonstrates the same pattern in Borden's model, but the crack width is more significant. The difference is caused by the chosen length parameter.

In the first step, the results from the chosen mean value of material properties are compared to the former publications for validation. The crack propagation plot is a vital tool for checking the correctness of numerical model. As shown in Fig. 4, the 3D crack propagation demonstrates the same pattern in Borden's model, but the crack width is

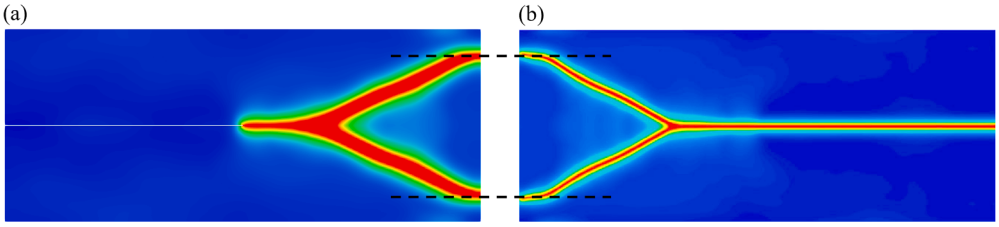

Fig. 4. Crack propagation plots of dynamic branching test at $t = 80$ μs: (a) proposed 3D model; (b) Borden's results [40].

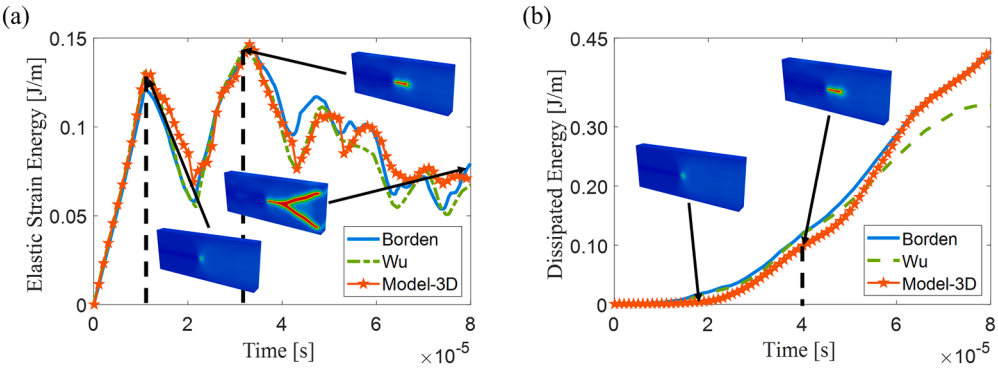

Fig. 5. Energy plots of dynamic branching test, along with results by Borden et al. [40] and Nguyen and Wu [71]: (a) Elastic strain energy; (b) dissipated energy.

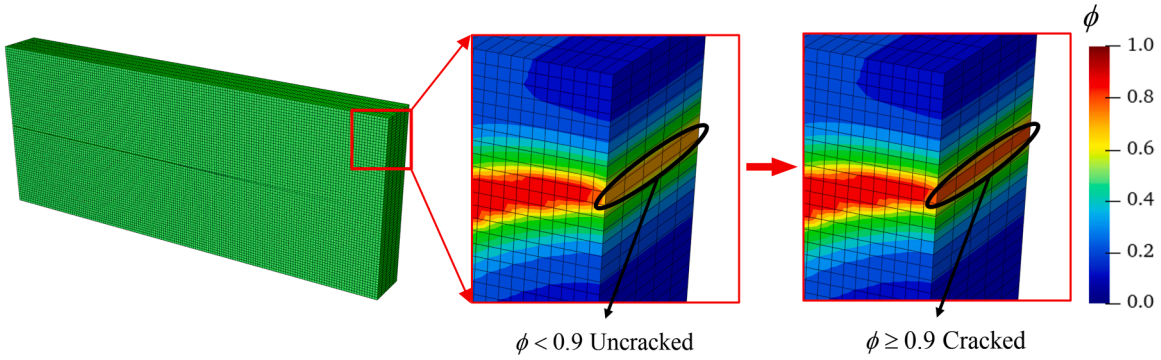

Fig. 6. Material status criteria: material is considered cracked when ϕ is greater than 0.9.

more significant. The difference is caused by the chosen length parameter.

Additionally, elastic strain and dissipated energy plots are plotted and compared with results in [40,71], as shown in Fig. 5. The relative error amongst the results can be acceptable because a coarser mesh setting is adopted in the simulated 3D model.

Then, variabilities are introduced into the simulation. A total of 1000 full-scale Monte Carlo simulation cycles are performed as reference results of non-deterministic fracture responses.

The crack propagation plot demonstrates the phase field value distribution over the geometry. The material is defined as cracked if the phase field value is more significant than 0.9. Thus, it can be clearly determined how far the crack develops by finding all the nodes with $\phi > 0.9$. Numerically, all the nodal phase field values can be accessed by compiling post-processing Python codes with Abaqus and then damage assessments can be efficiently carried out.

In this study, two characteristic fracture behaviors, namely the full collapse time and the crack length at a specific time (50 μs), were investigated.

The assumption was made that the structure maintains its strength before fully collapsing. The time is extracted by determining whether the phase field values of the right boundary reach 0.9. As shown in Fig. 6, the crack propagated from the intact material to the cracked one. Then, the full collapse time from 1000 MCS is collected as the output while the inputs are variational material properties. The training data, including inputs and outputs, are adopted for virtual modelling with the X-SVR method. The convergence study showed that the deviation between X-SVR predictions and MCS results decreased to an acceptable gap when the training size was increased to 400 out of 1000. The plot of the probability density function and cumulative distribution function of full collapse time is illustrated in Fig. 7 (a–c) to show the accuracy of the proposed implementations.

From the serviceability perspective, the crack length is the widely accepted characterization. To eliminate the influence of branching, only the horizontal crack length is considered in this example.

The algorithm for calculating the horizontal crack length is: (1) finding all the nodes with a phase field value greater than 0.9 at a particular time; (2) extracting the horizontal coordinates of these selected nodes; (3) determining the maximum value of horizontal coordinates. A post-processing Python code was compiled and adopted in this numerical investigation following this algorithm. The crack lengths from 1000 MCS were collected as outputs, while the inputs were pre-set variational material properties. Similarly, the X-SVR method is adopted to derive the virtual model of the relationship between horizontal crack

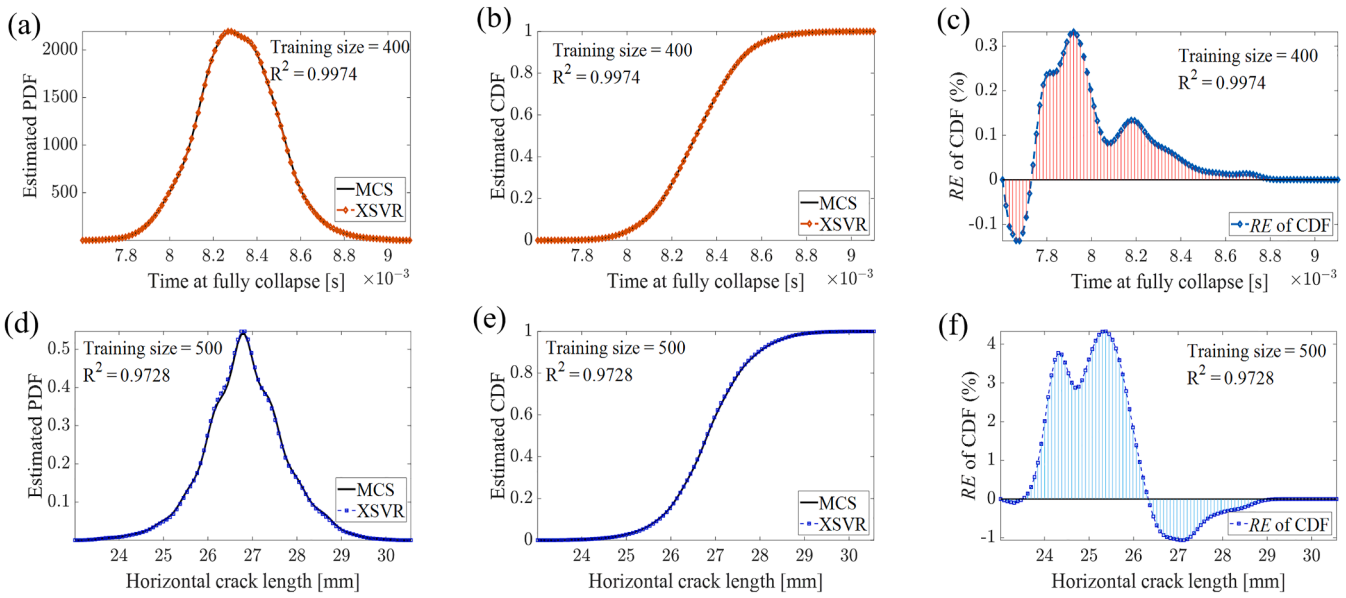

Fig. 7. Statistic information of dynamic branching test: (a) estimated PDF of full collapse time prediction, (b) estimated CDF of full collapse time prediction, (c) relative error of CDF of full collapse time prediction; (d) estimated PDF of horizontal crack length prediction, (e) estimated CDF of horizontal crack length prediction, (f) relative error of CDF of horizontal crack length prediction.

Table 3
Dynamic branching test: new material property sets.

Material properties	Set 1	Set 2
ρ [kg/m^3]	2148	2539
E [GPa]	2.95e10	3.42e10
υ	0.186	0.225
G_c [J/m^2]	2.88	3.11

length and variational material properties. According to the convergence study, the deviation between predictions from the virtual model and MCS results decreased significantly when the training size reached 500 out of 1000. The plot of the probability density function and cumulative distribution function of the horizontal crack length is illustrated in Fig. 7 (d–f).

Finally, two new sets of material properties are introduced to show the virtual model's capability of predicting dynamic brittle fracture responses. The results of the trained virtual model are compared to the results of Abaqus simulations. The detailed input information is listed in Table 3.

The trained virtual model enables rapid prediction of fracture responses, such as full collapse time and horizontal crack length. The predicted results can be easily compared to Abaqus simulations for both material sets. In Table 4, the collapse time of models with new material properties is demonstrated. In the meantime, the computational time for them is listed as well. The relative error can be considered as very low considering the huge improvement in computational efficiency.

Furthermore, the predicted horizontal crack length comparison is also shown in Fig. 8. The relative error between the numerical and virtual models is limited to about 1%. In the meantime, the

Table 4
Predicted full collapse time for two new material property input sets.

Material properties	Set 1			Set 2		
Model	Virtual model	Abaqus	Relative error	Virtual model	Abaqus	Relative error
Full collapse time [s]	7878	7814	0.82%	8154	8146	0.098%
Computation time [s]	<1	15,568		<1	16,254	

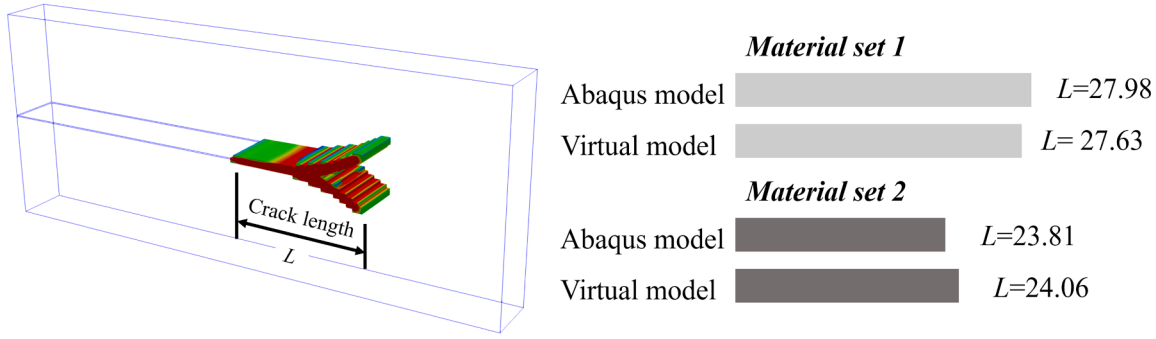

Fig. 8. Comparison of crack propagation predictions in two new material property input sets of dynamic branching test: the relative errors between two models are 1.25% in set 1 and 1.05% in set 2.

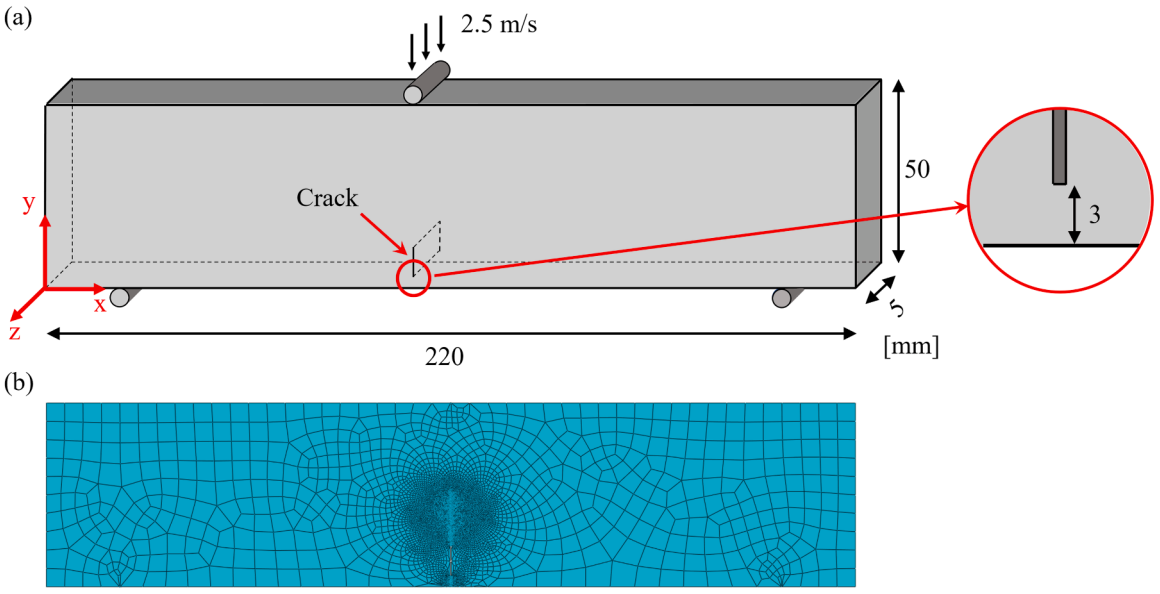

Fig. 9. (a) Geometric and boundary information of dynamic TPB test; (b) front view of meshed geometry model in ABAQUS.

computational cost is almost eliminated in the case of the virtual model. The virtual model only takes 0.3% of the time to complete the simulation and provides reliable crack propagation prediction. Therefore, the trained virtual model can accurately and rapidly deliver fracture response predictions with new variational inputs.

In this example, the validation of the benchmark problem, dynamic branching, is fully demonstrated in the first. The detailed application process of the proposed virtual modelling framework is then provided, following the sequence of identifying variabilities, calculating training data, training virtual model, and predicting by virtual model.

The numerical results from phase field model and virtual model are carefully analysed. Two characteristic fracture responses, the full collapse time and the crack length, are established based on ultimate strength and serviceability scenario respectively. It can be found in these two cases that the well-trained virtual model is capable of predicting fracture responses at a very fast speed by omitting complex physical formula. However, the great improvement in computational efficiency does not draw back the accuracy of fracture analysis from the comparison in both scenarios. To provide more illustrations of the proposed virtual modelling framework, another numerical examples is analysed next.

5.2. Dynamic three-point-bending test

In this section, dynamic three-point bending (TPB) test of beam with defect is investigated. The experiment setting is introduced in [72]. A caustic system with a high-speed camera is designed to investigate the fracture mechanism of Polymethyl methacrylate (PMMA) under dynamic loading. Based on the experimental results, PMMA can be considered a brittle material [73] and a 3D numerical model of the experiment is constructed in order to compare the fracture patterns.

The geometry and boundary conditions in numerical model are demonstrated in Fig. 9. The same as static three-point bending test, two support at the bottom side are fixed in vertical direction and the midpoint of upper boundary is impacted by the load. The dynamic load is simulated by a linear displacement. The velocity of the applied load remains at 2.5 m/s constantly throughout the simulation.

The mechanical performance of PMMA is enhanced by the interface between the carbon nanotube and the copolymer [74]. The unstable component density will introduce the variabilities in material properties in this case. In this section, material variabilities are considered in numerical model. For verification purposes, the mean values of non-deterministic material properties are chosen the same as [72]. The critical fracture release rate is not provided in the previous literature, so a specific number is selected for validation simulation.

Table 5
Variational material properties of dynamic TPB test.

Variational parameters	Mean	Standard deviation	Distribution type	Range
ρ [kg/m^3]	1200	20	Normal	/
E [GPa]	6.1e9	1.4e9	Lognormal	/
υ	0.31	/	Uniform	[0.306, 0.314]
G_c [J/m^2]	0.7	/	Uniform	[0.68, 0.72]

The detailed information of variabilities is listed in Table 5. The mesh of this model is refined in the possible crack path, which locates in the middle of span. The minimum mesh size in the whole geometry is 0.15 mm, so the length parameter is set as 0.3 mm to meet the requirements in phase field theory. There's a total of 62,440 nodes and 30,300 quadrangle elements in the model. The time increment is $\Delta t = 1 \times 10^{-8}$ s while the total simulation time $t_{\text{total}} = 8 \times 10^{-5}$ s.

In this analysis, the crack propagation plots generated by numerical models are compared to the experimental results. It is observed that the crack propagates from the bottom of the pre-crack and approaches the bottom boundary of the beam. Subsequently, a new upper crack starts to propagate towards the upper boundary. For calculation efficiency, the numerical simulation is stopped when the crack develops to the middle of the beam height. The comparison between the numerical model and experimental results is presented in Fig. 10, and it is evident that the crack patterns predicted by the model match the experiment closely.

To ensure the accuracy and effectiveness of the proposed virtual fracture analysis framework, we conducted a total of 1000 full-scale Monte Carlo simulations as the training sample for the virtual model. Two engineering applications were studied based on the framework's definition in the previous section.

The first concern is the time T_1 when the bottom crack reaches bottom boundary of the beam. In this case, the time represents the redundancy before the upper crack initializes and it will guide the engineer to design more outstanding strength beyond the standard limits. The second application analysed the depth of the crack propagation within a fixed time, specifically estimating and analysing the length of the upper crack, L_1. Similarly, the crack length is extracted by finding

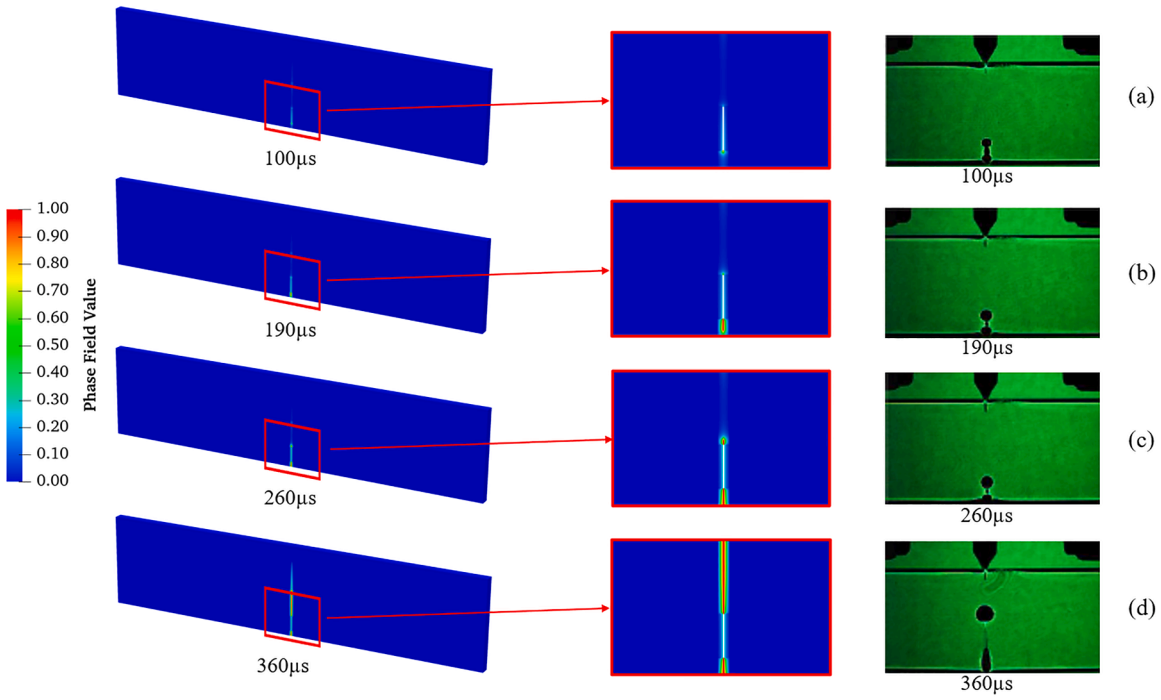

Fig. 10. Comparison of crack propagation in dynamic TPB test by Abaqus model and experimental results: (a) Initialization of bottom crack (b) Propagation of bottom crack (c) Initialization of upper crack (d) Propagation of upper crack. (3D model and its front view are provided for better illustration).

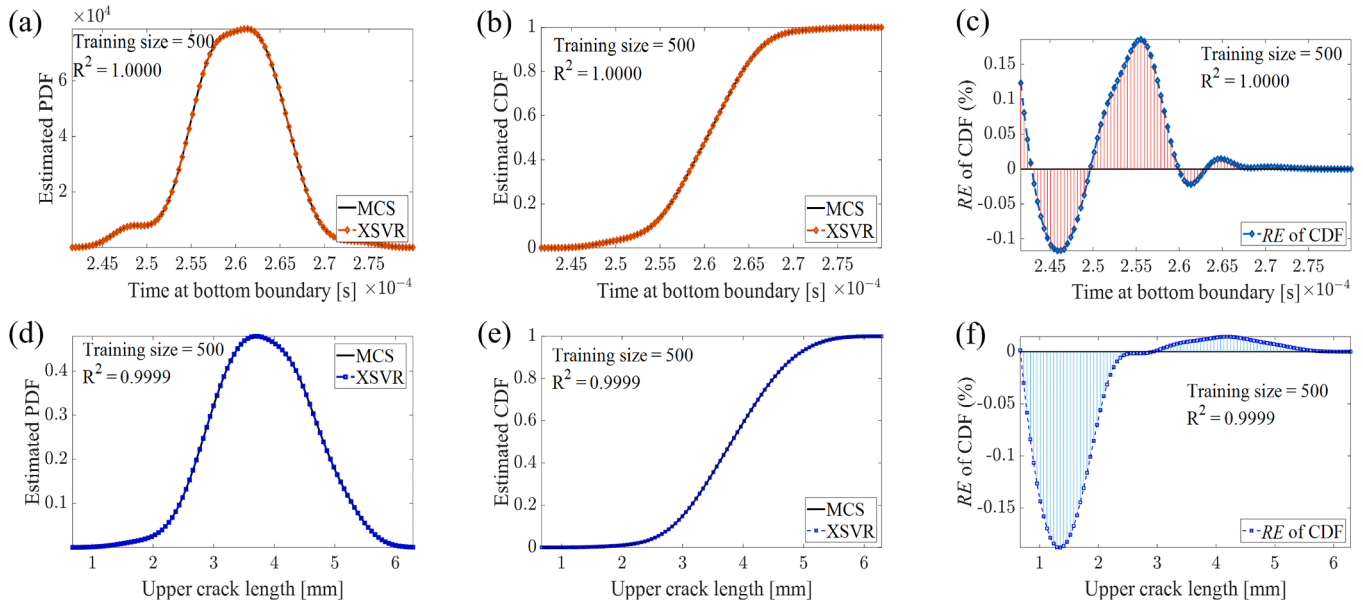

Fig. 11. Statistic information of two scenarios of dynamic TPB test: (a) estimated PDF of crack arrival time prediction, (b) estimated CDF of crack arrival time prediction, (c) relative error of CDF of crack arrival time prediction; (d) estimated PDF of upper crack length prediction, (e) estimated CDF of upper crack length prediction, (f) relative error of CDF of upper crack length prediction.

the maximum value of y-coordinates from all the cracked nodes.

For the mentioned two cases, 1000 MCS results of T_1 and L_1 are stored and adopted as training data for the virtual modelling framework. Based on the X-SVR method, the well-trained virtual model can predict the fracture responses like T_1 and L_1 accurately. A convergency study is conducted and the training sample size for two cases are set as 500. The plots of probability density function and cumulative distribution function of T_1 and L_1 are illustrated in Fig. 11.

With the trained virtual fracture model of PMMA, the crack propagation can be easily predicted with given material properties. In Table 6,

Table 6
Dynamic TPB test: two new material property sets.

Material properties	Set 1	Set 2
ρ [kg/m^3]	1150	1235
E [GPa]	5.95e9	6.3e9
υ	0.298	0.318
G_c [J/m^2]	0.675	0.731

Table 7
Dynamic TPB test: comparison of crack arrival time for two material property input sets.

Material properties	Set 1			Set 2		
Model type	Virtual model	Abaqus	Relative error	Virtual model	Abaqus	Relative error
Arrival time at bottom boundary [μs]	259.72	259.24	0.185%	261.43	261.37	0.023%
Computation time [s]	<1	6418	/	<1s	6661	/

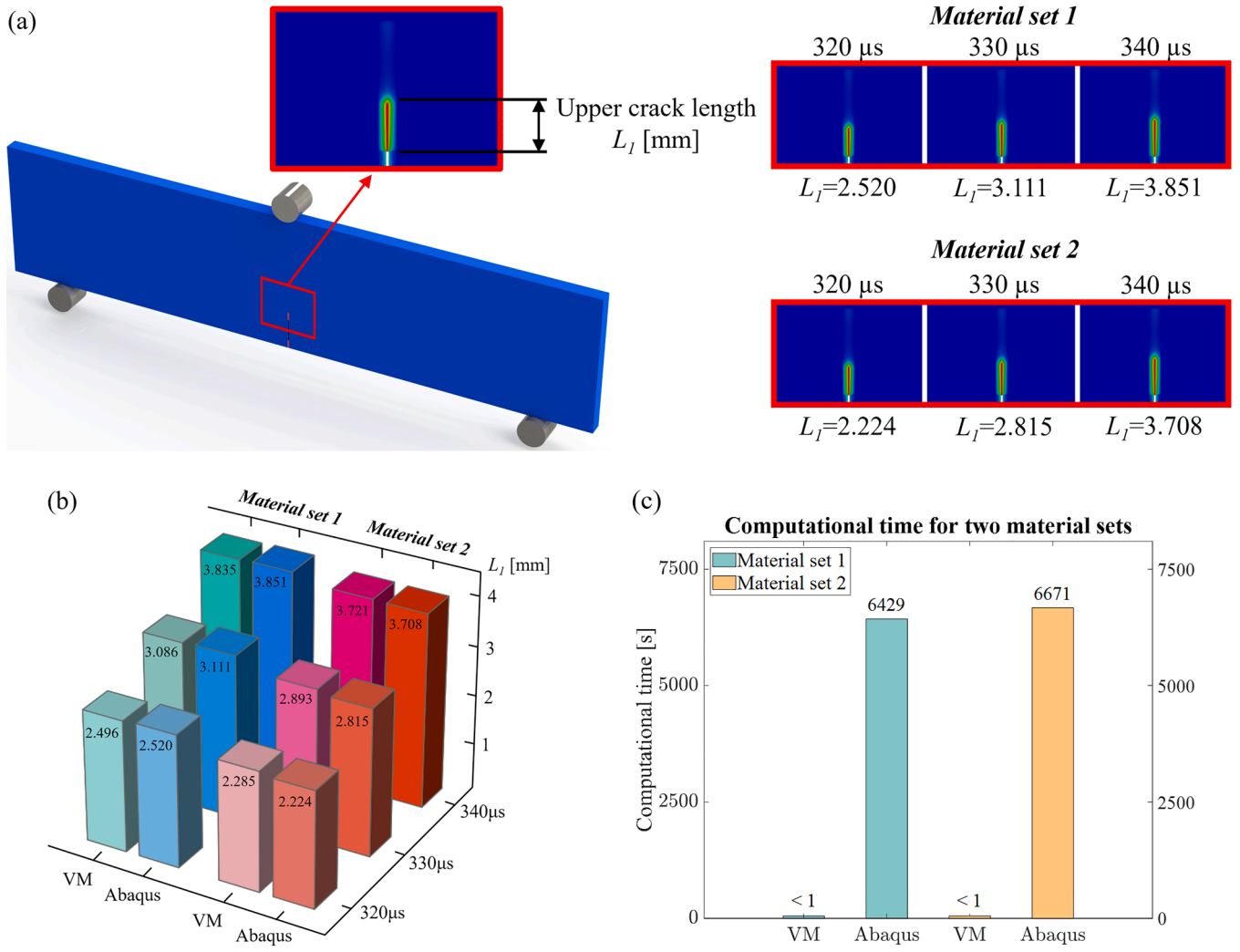

Fig. 12. (a) Upper crack length predictions of dynamic TPB test by Abaqus model at three different time; (b) comparison of upper crack length predictions by virtual model (VM) and Abaqus model; (c) comparison of computational time by virtual model (VM) and Abaqus model.

two new sets of material properties are chosen beyond the original variation range to demonstrate the feasibility of proposed framework. Both T_1 and L_1 are then predicted to discover the difference between virtual model and numerical model. The virtual model eliminates the computational time spent on calculation while maintaining the calculation accuracy within an acceptable level.

The simulated results of crack arrival time at bottom boundary T_1 by virtual model and Abaqus model are given in Table 7. The Abaqus model is assumed to give more accurate results because the virtual model is trained by Abaqus MCS outputs. For both of two new material property sets, the virtual model can predict the crack arrival time in a convincible way and the relative errors are limited to a tiny scale. In the meantime, the computational time of two different models is compared in Table 7 as well. The well-trained virtual model finishes the prediction within 1 s, while the Abaqus model takes about 2 h to complete the simulation.

The upper crack length L_1 is also simulated by two models for performance comparison. Three moments, which are 320 μs, 330 μs and 340 μs, are selected to show the crack propagation and the prediction verification. The upper crack continues to develop in the middle line of beam span after the lower crack reaches the bottom boundary. In both material sets, the crack propagations by Abaqus model are clearly shown in Fig. 12(a). The comparison 3D bar plot in Fig. 12(b) shows that the difference between virtual model and Abaqus model can be considered slight. However, the computational time of two methods has an enormous gap, which is evident in Fig. 12(c).

In this example, the dynamic three point bending test is analysed numerically and compared to experimental results. The patterns of crack propagation agree with the experiments and fully simulated the fracture behaviour in a numerical way. Similarly, two different fracture responses are selected in a quantitative way and the training data is generated. The successful training of virtual model provides reliable fracture predictions.

Therefore, the proposed virtual fracture analysis framework enables rapid and accurate prediction of dynamic fracture responses, such as crack initiation and length. This framework has the potential to be extended to fracture assessment. For example, the repeating experimental test model can be partly simulated by phase field to acquire sufficient data for calculating fracture toughness. Additionally, the virtual modelling technique enables reliability analysis to be conducted within a short time, offering the possibility of a rapid testing facility to assess the health status of structural components in critical infrastructures. This capability inspires confidence in the public and enhances safety under unexpected environmental hazards.

6. Conclusions

In this paper, a non-deterministic phase field virtual modelling framework specifically designed for dynamic brittle fracture analysis is proposed. The material property variabilities that can lead to instability in real-life conditions are taken into account, which is crucial for accurate simulations. The virtual modelling framework aims to circumvent the time-consuming fracture simulations, which are often encountered in physical phase field formulations, by training a virtual model to predict dynamic fracture responses.

One of the major achievements of this work is the successful application of the novel X-SVR method with a T-spline polynomial kernel in training the virtual model. The virtual model represents the virtual governing relationship between the system inputs and fracture responses. By adopting the virtual modelling technique, the computational efficiency of predicting fracture responses is significantly improved. Moreover, the virtual phase field model has proven capable of providing stable and accurate results in comparison to the phase field method model, even when faced with variabilities outside of the original training ranges. The enhanced accuracy and efficiency of our virtual modelling framework holds potential for establishing a reliability and structural safety database, which is a critical aspect of engineering applications. The satisfactory performance of the proposed framework is demonstrated in two three-dimensional numerical examples, with detailed comparisons provided to prove its accuracy and robustness. By adopting multiple fracture failure criteria based on real-world engineering scenarios, the framework's workflow is visualized and demonstrated. It's essential to mention that this paper concentrates exclusively on brittle materials. Additional research is needed in the future to create a broader non-deterministic phase field virtual modelling framework.

In conclusion, by employing this framework, engineers can obtain timely fracture predictions with continuously varying system inputs, enabling a more efficient and effective analysis. The application of the framework also ensures that potential fracture responses can be identified and addressed early in the process, reducing the risk of overall structural failures.

CRediT authorship contribution statement

Yiyang Liu: Conceptualization, Software, Methodology, Writing – original draft. **Yuan Feng:** Conceptualization, Software, Methodology, Writing – review & editing. **Di Wu:** Writing – review & editing, Supervision, Methodology. **Xiaojun Chen:** Supervision, Methodology. **Wei Gao:** Writing – review & editing, Supervision, Methodology.

Declaration of Competing Interest

The authors declare that they have no known competing financial interests or personal relationships that could have appeared to influence the work reported in this paper.

Data availability

No data was used for the research described in the article.

Acknowledgments

This research is fully funded by Australia Research Council projects IH210100048, IH200100010 and DP210101353. The author Yiyang Liu is funded by Australian Government Research Training Program Scholarship (RTP).

Appendix A. Definitions of vectors and matrices defined in the optimization problem

The other matrices in the X-SVR optimization problem are defined as:

$$\widehat{\mathbf{D}}_x = \begin{bmatrix} \delta_1\mathbf{I}_{j\times j} & & & \\ & \delta_1\mathbf{I}_{j\times j} & & \\ & & z\mathbf{I}_{j\times j} & \\ & & & z\mathbf{I}_{j\times j} \end{bmatrix} \tag{A-1}$$

$$\widehat{\mathbf{K}}_m = \begin{bmatrix} \mathbf{0}_{2j\times 2j} & \mathbf{0}_{2j\times j} & \mathbf{0}_{2j\times j} \\ \mathbf{0}_{j\times 2j} & \mathbf{I}_{j\times j} & \mathbf{0}_{j\times j} \\ \mathbf{0}_{j\times 2j} & \mathbf{0}_{j\times j} & -\mathbf{I}_{j\times j} \end{bmatrix} \tag{A-2}$$

$$\widehat{\mathbf{S}}_m = \begin{bmatrix} \mathbf{0}_{2j\times j} & \mathbf{0}_{2j\times j} & \mathbf{0}_{2j\times 2j} \\ -\mathbf{W}_{train} & \mathbf{W}_{train} & \mathbf{0}_{j\times 2j} \\ \mathbf{W}_{train} & -\mathbf{W}_{train} & \mathbf{0}_{j\times 2j} \end{bmatrix} \tag{A-3}$$

$$\mathbf{b}_x = \begin{bmatrix} \mathbf{e}_j \\ \mathbf{e}_j \\ \mathbf{0}_{2j} \end{bmatrix}, \widehat{\mathbf{e}}_x = \begin{bmatrix} \mathbf{0}_{2j} \\ \mathbf{e}_j \\ \mathbf{e}_j \end{bmatrix}, \widehat{\mathbf{v}}_x = \begin{bmatrix} \mathbf{0}_{2j} \\ \mathbf{y}_{train} \\ -\mathbf{y}_{train} \end{bmatrix}, \mathbf{t}_x = \begin{bmatrix} \mathbf{p}_x \\ \mathbf{q}_x \\ \theta \\ \widehat{\theta} \end{bmatrix} \tag{A-4}$$

References

[1] Chen X. Fracture of wind turbine blades in operation-Part I: a comprehensive forensic investigation. Wind Energy 2018;21:1046–63. https://doi.org/10.1002/we.2212.

[2] Marín JC, Barroso A, París F, Cañas J. Study of fatigue damage in wind turbine blades. Eng Fail Anal 2009;16:656–68. https://doi.org/10.1016/j.engfailanal.2008.02.005.

[3] Zhang P, Hu X, Bui TQ, Yao W. Phase field modeling of fracture in fiber reinforced composite laminate. Int J Mech Sci 2019;(105008):161–2. https://doi.org/10.1016/j.ijmecsci.2019.07.007.

[4] Khosravani MR, Wagner P, Fröhlich D, Weinberg K. Dynamic fracture investigations of ultra-high performance concrete by spalling tests. Eng Struct 2019;201:109844. https://doi.org/10.1016/j.engstruct.2019.109844.

[5] Zhang Y, Sun J, Liu C, Hou X, Wang J. Phase field modeling of coupling evolution of fracture and dielectric breakdown in ferroelectric materials. Int J Mech Sci 2022;236:107747. https://doi.org/10.1016/j.ijmecsci.2022.107747.

[6] Ben Othmen K, Haddar N, Jegat A, Manach PY, Elleuch K. Ductile fracture of AISI 304 L stainless steel sheet in stretching. Int J Mech Sci 2020;172:105404. https://doi.org/10.1016/j.ijmecsci.2019.105404.

[7] Kim JS, Kim YJ, Lee MW, Kim KS, Shibanuma K. Fracture simulation model for API X80 Charpy test in ductile-brittle transition temperatures. Int J Mech Sci 2020;182:105771. https://doi.org/10.1016/j.ijmecsci.2020.105771.

[8] Kacem A, Laurent H, Thuillier S. Experimental and numerical investigation of ductile fracture for AA6061-T6 sheets at room and elevated temperatures. Int J Mech Sci 2022;222:107201. https://doi.org/10.1016/j.ijmecsci.2022.107201.

[9] Bažant ZP, Dönmez AA, Nguyen HT. Précis of gap test results requiring reappraisal of line crack and phase-field models of fracture mechanics. Eng Struct 2022;250:113285. https://doi.org/10.1016/j.engstruct.2021.113285.

[10] Sidharth R, Nikhil R, Krishnan SA, Keralavarma SM, Moitra A, Vasudevan M. Crack initiation and growth in 316LN stainless steel: experiments and XFEM simulations. Eng Fract Mech 2022;274:108770. https://doi.org/10.1016/j.engfracmech.2022.108770.

[11] Cui Y, Zeng X, Tan VBC, Zhang Z. Experimental and numerical studies of NiTi dynamic fracture behaviors under the impact loading. Int J Mech Sci 2022;235:107724. https://doi.org/10.1016/j.ijmecsci.2022.107724.

[12] Griffith AA, Taylor VI GI. The phenomena of rupture and flow in solids. Philos Trans R Soc Lond Ser A 1921;221:163–98. https://doi.org/10.1098/rsta.1921.0006. Containing Papers of a Mathematical or Physical Character.

[13] Irwin GR. Analysis of stresses and strains near the end of a crack traversing a plate. J Appl Mech 1957;24:361–4. https://doi.org/10.1115/1.4011547.

[14] Belytschko T, Black T. Elastic crack growth in finite elements with minimal remeshing. Int J Numer Methods Eng 1999;45:601–20. https://doi.org/10.1002/(SICI)1097-0207(19990620)45:5<601AID-NME598>3.0.CO;2-J.

[15] Moës N, Dolbow J, Belytschko T. A finite element method for crack growth without remeshing. Int J Numer Methods Eng 1999;46:131–50. https://doi.org/10.1002/(SICI)1097-0207(19990910)46:1<131. AID-NME726>3.0.CO;2-J.

[16] Simo JC, Oliver J, Armero F. An analysis of strong discontinuities induced by strain-softening in rate-independent inelastic solids. Comput Mech 1993;12:277–96. https://doi.org/10.1007/BF00372173.

[17] Fries TP, Belytschko T. The extended/generalized finite element method: an overview of the method and its applications. Int J Numer Methods Eng 2010;84:253–304. https://doi.org/10.1002/nme.2914.

[18] Egger A, Pillai U, Agathos K, Kakouris E, Chatzi E, Aschroft IA, Triantafyllou SP. Discrete and phase field methods for linear elastic fracture mechanics: a comparative study and state-of-the-art review. Appl Sci 2019;9:2436. https://doi.org/10.3390/app9122436.

[19] Francfort GA, Marigo JJ. Revisiting brittle fracture as an energy minimization problem. J Mech Phys Solids 1998;46:1319–42. https://doi.org/10.1016/S0022-5096(98)00034-9.

[20] Aranson IS, Kalatsky VA, Vinokur VM. Continuum Field Description of Crack Propagation. Phys Rev Lett 2000;85:118–21. https://doi.org/10.1103/PhysRevLett.85.118.

[21] Bourdin B, Francfort GA, Marigo JJ. Numerical experiments in revisited brittle fracture. J Mech Phys Solids 2000;48:797–826. https://doi.org/10.1016/S0022-5096(99)00028-9.

[22] Borden MJ, Hughes TJR, Landis CM, Verhoosel CV. A higher-order phase-field model for brittle fracture: formulation and analysis within the isogeometric analysis framework. Comput Methods Appl Mech Eng 2014;273:100–18. https://doi.org/10.1016/j.cma.2014.01.016.

[23] Amor H, Marigo JJ, Maurini C. Regularized formulation of the variational brittle fracture with unilateral contact: numerical experiments. J Mech Phys Solids 2009;57:1209–29. https://doi.org/10.1016/j.jmps.2009.04.011.

[24] Miehe C, Hofacker M, Welschinger F. A phase field model for rate-independent crack propagation: robust algorithmic implementation based on operator splits. Comput Methods Appl Mech Eng 2010;199:2765–78. https://doi.org/10.1016/j.cma.2010.04.011.

[25] Miehe C, Welschinger F, Hofacker M. Thermodynamically consistent phase-field models of fracture: variational principles and multi-field FE implementations. Int J Numer Methods Eng 2010;83:1273–311. https://doi.org/10.1002/nme.2861.

[26] Ambati M, Gerasimov T, De Lorenzis L. A review on phase-field models of brittle fracture and a new fast hybrid formulation. Comput Mech 2015;55:383–405. https://doi.org/10.1007/s00466-014-1109-y.

[27] Wu JY, Huang Y, Zhou H, Nguyen VP. Three-dimensional phase-field modeling of mode I + II/III failure in solids. Comput Methods Appl Mech Eng 2021;373:113537. https://doi.org/10.1016/j.cma.2020.113537.

[28] Rabczuk T, Samaniego E. Discontinuous modelling of shear bands using adaptive meshfree methods. Comput Methods Appl Mech Eng 2008;197:641–58. https://doi.org/10.1016/j.cma.2007.08.027.

[29] Fang JG, Wu CQ, Li J, Liu Q, Wu C, Sun GY, Li Q. Phase field fracture in elasto-plastic solids: variational formulation for multi-surface plasticity and effects of plastic yield surfaces and hardening. Int J Mech Sci 2019;156:382–96. https://doi.org/10.1016/j.ijmecsci.2019.03.012.

[30] Fang J, Wu C, Rabczuk T, Wu C, Ma C, Sun G, Li Q. Phase field fracture in elasto-plastic solids: abaqus implementation and case studies. Theor Appl Fract Mech 2019;103:102252. https://doi.org/10.1016/j.tafmec.2019.102252.

[31] Seiler M, Linse T, Hantschke P, Kästner M. An efficient phase-field model for fatigue fracture in ductile materials. Eng Fract Mech 2020;224:106807. https://doi.org/10.1016/j.engfracmech.2019.106807.

[32] Ambati M, Gerasimov T, De Lorenzis L. Phase-field modeling of ductile fracture. Comput Mech 2015;55:1017–40. https://doi.org/10.1007/s00466-015-1151-4.

[33] Miehe C, Aldakheel F, Raina A. Phase field modeling of ductile fracture at finite strains: a variational gradient-extended plasticity-damage theory. Int J Plast 2016;84:1–32. https://doi.org/10.1016/j.ijplas.2016.04.011.

[34] Shi Q, Yu H, Guo L, Hao L, Huang K. A phase field model with plastic history field for fracture of elasto-plastic materials. Eng Fract Mech 2022;268:108447. https://doi.org/10.1016/j.engfracmech.2022.108447.

[35] Huang C, Gao X. Development of a phase field method for modeling brittle and ductile fracture. Comput Mater Sci 2019;169:109089. https://doi.org/10.1016/j.commatsci.2019.109089.

[36] Moshkelgosha E, Mamivand M. Three-dimensional phase field modeling of fracture in shape memory ceramics. Int J Mech Sci 2021;204:106550. https://doi.org/10.1016/j.ijmecsci.2021.106550.

[37] Cissé C, Asle Zaeem M. Transformation-induced fracture toughening in CuAlBe shape memory alloys: a phase-field study. Int J Mech Sci 2021;192:106144. https://doi.org/10.1016/j.ijmecsci.2020.106144.

[38] Simoes M, Martínez-Pañeda E. Phase field modelling of fracture and fatigue in Shape Memory Alloys. Comput Methods Appl Mech Eng 2021;373. https://doi.org/10.1016/j.cma.2020.113504.

[39] Karma A, Kessler DA, Levine H. Phase-field model of mode III dynamic fracture. Phys Rev Lett 2001;87:045501. https://doi.org/10.1103/PhysRevLett.87.045501.

[40] Borden MJ, Verhoosel CV, Scott MA, Hughes TJR, Landis CM. A phase-field description of dynamic brittle fracture. Comput Methods Appl Mech Eng 2012;217-220:77–95. https://doi.org/10.1016/j.cma.2012.01.008.

[41] Shi J, Chopp D, Lua J, Sukumar N, Belytschko T. Abaqus implementation of extended finite element method using a level set representation for three-dimensional fatigue crack growth and life predictions. Eng Fract Mech 2010;77:2840–63. https://doi.org/10.1016/j.engfracmech.2010.06.009.

[42] Msekh MA, Sargado JM, Jamshidian M, Areias PM, Rabczuk T. Abaqus implementation of phase-field model for brittle fracture. Comput Mater Sci 2015;96:472–84. https://doi.org/10.1016/j.commatsci.2014.05.071.

[43] Molnár G, Gravouil A. 2D and 3D Abaqus implementation of a robust staggered phase-field solution for modeling brittle fracture. Finite Elem Anal Des 2017;130:27–38. https://doi.org/10.1016/j.finel.2017.03.002.

[44] Molnár G, Gravouil A, Seghir R, Réthoré J. An open-source Abaqus implementation of the phase-field method to study the effect of plasticity on the instantaneous fracture toughness in dynamic crack propagation. Comput Methods Appl Mech Eng 2020;365:113004. https://doi.org/10.1016/j.cma.2020.113004.

[45] A. Ingraffea, M. Grigoriu. Probabilistic fracture mechanics: a validation of predictive capability. 1990; 155.

[46] Gerasimov T, Römer U, Vondřejc J, Matthies HG, De Lorenzis L. Stochastic phase-field modeling of brittle fracture: computing multiple crack patterns and their probabilities. Comput Methods Appl Mech Eng 2020;372:113353. https://doi.org/10.1016/j.cma.2020.113353.

[47] Feng Y, Wang Q, Wu D, Luo Z, Chen X, Zhang T, Gao W. Machine learning aided phase field method for fracture mechanics. Int J Eng Sci 2021;169:103587. https://doi.org/10.1016/j.ijengsci.2021.103587.

[48] Hammersley JM, Handscomb DC. Monte Carlo methods. Dordrecht: Springer; 1966. 978-94-009-5821-0.

[49] Fishman G. Monte Carlo: concepts, algorithms, and applications. Springer Science & Business Media; 2013. 1475725531.

[50] Seleš K, Lesičar T, Tonković Z, Sorić J. A residual control staggered solution scheme for the phase-field modeling of brittle fracture. Eng Fract Mech 2019;205:370–86. https://doi.org/10.1016/j.engfracmech.2018.09.027.

[51] Hirshikesh, Pramod ALN, Annabattula RK, Ooi ET, Song C, Natarajan S. Adaptive phase-field modeling of brittle fracture using the scaled boundary finite element method. Comput Methods Appl Mech Eng 2019;355:284–307. https://doi.org/10.1016/j.cma.2019.06.002.

[52] Krishnan UM, Gupta A, Chowdhury R. Adaptive phase-field modeling of brittle fracture using a robust combination of error-estimator and markers. Eng Fract Mech 2022;274:108758. https://doi.org/10.1016/j.engfracmech.2022.108758.

[53] Qiu S, Duan Q, Shao Y, Chen S, Yao W. Adaptive finite element method for hybrid phase-field modeling of three-dimensional cracks. Eng Fract Mech 2022;271:108636. https://doi.org/10.1016/j.engfracmech.2022.108636.

[54] Xu W, Li H, Li Y, Wang T, Lu S, Qiang S, Hua X. A phase field method with adaptive refinement strategy and virtual crack insertion technique. Eng Fract Mech 2022;271:108669. https://doi.org/10.1016/j.engfracmech.2022.108669.

[55] Tian F, Zhang M, Zeng J, Li B, Li L. Adaptive stabilized mixed formulation for phase field fracture modeling of nearly incompressible finite elasticity. Int J Mech Sci 2022;236:107753. https://doi.org/10.1016/j.ijmecsci.2022.107753.

[56] Cheon YJ, Kim HG. An adaptive material point method coupled with a phase-field fracture model for brittle materials. Int J Numer Methods Eng 2019;120:987–1010. https://doi.org/10.1002/nme.6167.
[57] Patil RU, Mishra BK, Singh IV. An adaptive multiscale phase field method for brittle fracture. Comput Methods Appl Mech Eng 2018;329:254–88. https://doi.org/10.1016/j.cma.2017.09.021.
[58] Baek H, Kweon C, Park K. Multiscale dynamic fracture analysis of composite materials using adaptive microstructure modeling. Int J Numer Methods Eng 2020;121:5719–41. https://doi.org/10.1002/nme.6521.
[59] Samaniego C, Ulloa J, Rodríguez P, Houzeaux G, Vázquez M, Samaniego E. A phase-field model for ductile fracture with shear bands: a parallel implementation. Int J Mech Sci 2021;200:106424. https://doi.org/10.1016/j.ijmecsci.2021.106424.
[60] Feng J, Liu L, Wu D, Li G, Beer M, Gao W. Dynamic reliability analysis using the extended support vector regression (X-SVR). Mech Syst Signal Process 2019;126:368–91. https://doi.org/10.1016/j.ymssp.2019.02.027.
[61] Feng Y, Wang Q, Wu D, Gao W, Tin-Loi F. Stochastic nonlocal damage analysis by a machine learning approach. Comput Methods Appl Mech Eng 2020;372:113371. https://doi.org/10.1016/j.cma.2020.113371.
[62] Griffith AA. The phenomena of rupture and flow in solids. Philos Trans R Soc Lond Ser A 1921;221:163–98. Containing Papers of a Mathematical or Physical Character.
[63] Freddi F, Royer-Carfagni G. Regularized variational theories of fracture: a unified approach. J Mech Phys Solids 2010;58:1154–74. https://doi.org/10.1016/j.jmps.2010.02.010.
[64] Rebba R, Mahadevan S. Computational methods for model reliability assessment. Reliab Eng Syst Saf 2008;93:1197–207. https://doi.org/10.1016/j.ress.2007.08.001.
[65] Goller B, Pradlwarter HJ, Schuëller GI. Reliability assessment in structural dynamics. J Sound Vib 2013;332:2488–99. https://doi.org/10.1016/j.jsv.2012.11.021.
[66] Drucker H, Burges CJ, Kaufman L, Smola A, Vapnik V. Support vector regression machines. Adv Neural Inf Process Syst 1996;9:155–61.
[67] Wang L, Zhu J, Zou H. The doubly regularized support vector machine. Stat Sin 2006;16:589–615.
[68] Li J, Cheng K, Wang S, Morstatter F, Trevino RP, Tang J, Liu H. Feature selection: a data perspective. ACM Comput Surv (CSUR) 2017;50. https://doi.org/10.1145/3136625.
[69] Tang Y, Guo W, Gao J. Efficient model selection for support vector machine with Gaussian kernel function. In: Proceedings of the IEEE symposium on computational intelligence and data mining; 2009. p. 40–5. https://doi.org/10.1109/CIDM.2009.4938627.
[70] Lestari B, Fatmawati, Budiantara IN, Chamidah N. Estimation of regression function in multi-response nonparametric regression model using smoothing spline and kernel estimators. J Phys Conf Ser 2018;1097:012091. https://doi.org/10.1088/1742-6596/1097/1/012091.
[71] Nguyen VP, Wu JY. Modeling dynamic fracture of solids with a phase-field regularized cohesive zone model. Comput Methods Appl Mech Eng 2018;340:1000–22. https://doi.org/10.1016/j.cma.2018.06.015.
[72] Xue Y, Cheng Y, Li Q, Wang K, Xu W, Du W. Research on dynamic failure mechanism of three-point bending beam with joint. Mech Adv Mater Struct 2022:1–24. https://doi.org/10.1080/15376494.2022.2028041.
[73] Sharon E, Fineberg J. Microbranching instability and the dynamic fracture of brittle materials. Phys Rev B 1996;54:7128–39. https://doi.org/10.1103/PhysRevB.54.7128.
[74] Ali U, Karim KJBA, Buang NA. A review of the properties and applications of Poly (Methyl Methacrylate) (PMMA). Polym Rev 2015;55:678–705. https://doi.org/10.1080/15583724.2015.1031377.